Lai *et al.*
Protection and Control of Modern Power Systems (2023) 8:42
https://doi.org/10.1186/s41601-023-00316-8

Protection and Control of Modern Power Systems

ORIGINAL RESEARCH

Open Access

Typology and working mechanism of a hybrid power router based on power-frequency transformer electromagnetic coupling with converters

Jinmu Lai[1], Xin Yin[2*], Xianggen Yin[3], Jiaxuan Hu[3] and Fan Xiao[4]

Abstract

The power router (PR) is a promising piece of equipment for realizing multi-voltage level interconnection and flexible power control in the future distribution power grid. In this paper, a hybrid PR (HPR) topology based on power-frequency transformer electromagnetic coupling with converters is proposed for the medium distribution power grid. The power-frequency transformer is used to undertake power transmission, voltage conversion, and other main tasks, while the power electronic converters are combined to achieve active control. Equivalent magnetic and electrical circuit models are established to help discuss the operating principle of the proposed HPR. Additionally, the power flow and control principle of the HPR in different operating conditions are analyzed, with the control system design scheme presented. The theoretical analysis results are verified by MATLAB/Simulink + Plecs simulation and a controller hardware-in-the-loop study, as well as a down-scale experimental test, indicating that the proposed HPR is flexible in active voltage support and current control.

Keywords Power router, Power-frequency transformer, Power electronic converter, Hybrid, Working mechanism

1 Introduction

Owing to uncontrollability, lack of fault isolation and fault ride-through capabilities, as well as other shortcomings, it is challenging for conventional transformers to actively control and optimize the operation of distribution power grids, where nonintelligent techniques, such as bus tie switch and transformer tapping, are mainly adopted to control node voltages and power flows [1]. Additionally, complex grid faults can cause transient disturbances [2], such as unbalanced voltage dip or swell. These can critically affect the safe connection and operation of distributed renewable energy, microgrid, and load. Numerous off-grid events of distributed generation (DG) equipment have been reported. A power router (PR) is significant for renewable DG connection, multi-voltage flexible interconnection, and multi-port power control, and can notably boost the renewable DG accommodation capacity and continuous power supply capacity of distribution grids, to meet the urgent demand for flexible control and reliable power supply of power distribution grids caused by high penetration of renewable energy sources and power electronic equipment [3].

The PRs currently used for medium-voltage and medium-power conversion in power distribution grids

*Correspondence:
Xin Yin
leoxinyin@qq.com
[1] School of Electrical and Information Engineering, Zhengzhou University, Zhengzhou 450001, Henan Province, People's Republic of China
[2] School of Automation, Wuhan University of Technology, Wuhan 430070, Hubei Province, People's Republic of China
[3] School of Electrical and Electronic Engineering, Huazhong University of Science and Technology (HUST), Wuhan 430074, Hubei Province, People's Republic of China
[4] State Grid Hubei Electric Power Research Institute, Wuhan 430077, Hubei Province, People's Republic of China

use cascaded H-bridge (CHB) typology [4] or modular multilevel converter (MMC) typology [5]. A CHB-based PR topology is proposed by the Future Renewable Electric Energy Delivery and Management System of North Carolina State University [4]. Its main circuit uses an input-series output-parallel (ISOP) topology, which comprises a medium-voltage stage CHB, an isolation stage with ISOP dual active bridge (ISOP-DAB), and a low-voltage stage DC/AC inverter. This design meets the fundamental function requirements for PRs. An auto-balancing electronic power transformer (EPT) topology, which decouples the mutual influence of the three-phase imbalance between the high- and low-voltage sides of the EPT by an interleaving design, is proposed in [6]. The aforementioned topologies [4, 6] use the CHB on the medium-voltage side. Reference [7] proposes an MMC-based PR topology, which comprises a medium-voltage stage MMC, an isolation stage with ISOP-DAB, and a low-voltage stage DC/AC inverter. These can realize the interconnection of medium-voltage AC (MVAC) and DC distribution networks. Several studies have shown the enhancement of the techno-economic aspects of the full power electronic converters (PEC) module-based PR through structural optimization [8] or control improvement [9] to achieve certain beneficial effects.

CHB- and MMC-based PRs integrate functions, such as voltage conversion, power control, fault isolation, and power quality control, and have become paramount equipment for integrating and optimizing various PEC equipment in power grids, and improving the intelligent power grid management level. Nevertheless, these topologies require numerous PEC modules, and there are still several challenges in replacing power-frequency (PF) transformers with PRs in AC power distribution grids, particularly the high cost, high loss, and complex typology of CHB- and MMC-based PRs (e.g., 1 MVA 10 kV / 400 V PR). They have more than five times the cost and three times the loss of a PF transformer [10]. This poor techno-economic performance inhibits the widespread application of PRs to this day.

Compared with the CHB- and MMC-based PRs scheme, the hybrid scheme of the PF transformer and PEC is a potential direction for PR development. An integrated transformer design scheme based on the inductive filtering principle, which is designed with an extended delta winding on the secondary side for the parallel connection of the converter and realizes current control using the magnetic flux balance principle, is proposed in [11, 12]. Nevertheless, this scheme is used only for power quality control. An integrated transformer design scheme based on a multi-winding tap connection is proposed in [13, 14], in which the center tap is drawn from the medium-voltage side winding of the transformer for the connection of the converter. This scheme is also used for power quality control. However, it is difficult for these integrated schemes of a PF transformer in parallel with a converter [11–14] to realize active voltage regulation, and they fail to meet the flexible control requirement for PRs.

Thus, a next generation distribution transformer, which comprises two windings on the secondary side with one connected to an AC/AC converter in series, is proposed in [15]. This structure is further optimized in [16] and extended to a three-phase structure [17]. A transformer-integrated dynamic voltage regulator, which realizes the dynamic voltage amplitude and phase angle adjustment of the secondary side by controlling the amplitude and phase angle of the output voltage of the AC/DC/AC converter, is proposed in [18]. However, the voltage amplitude and phase angle adjustment ranges of the transformer are narrow, and all transmitted power flows through the connected AC/DC/AC converter, thereby increasing the operating power loss and reducing operating efficiency and reliability. A new type of PR with series-shunt architecture is constructed in [19], in which the series PEC is connected to the AC grid in series through the transformer and the shunt PEC is connected to an AC bus in parallel. A transformer-integrated back-to-back converter scheme, which realizes the simultaneous correction of voltage and current power quality, is proposed in [20]. A multi-winding integrated three-phase hybrid transformer with series–shunt three-phase two-level converters connected by the secondary winding on the low-voltage side is proposed in [21, 22]. In addition, references [23, 24] propose an improved hybrid distribution transformer, though this structure requires an additional series transformer on the medium-voltage side, thereby increasing complexity and cost.

In this paper, a hybrid PR (HPR) based on PF transformer electromagnetic coupling with PECs is proposed, one which combines the benefits of the PF transformer and PEC. The core idea of the proposed HPR is that it uses the PF transformer to undertake the voltage conversion, power transmission, and the low-voltage PEC to realize the flexible active control function. The equivalent magnetic and electrical circuit models are established to expound the HPR's operating principle. In addition, with the control scheme presented, the power flow and control strategy of the HPR in different operating conditions are analyzed. Finally, the feasibility of the proposed HPR is verified by Simulink + Plecs simulation, controller hardware-in-the-loop (CHIL) and down-scale experimental test results.

2 HPR topology and its wiring scheme

The proposed HPR topology is shown in Fig. 1, where the PF transformers are used for the main power transmission and the converters are used for the active voltage and current adjustment. The proposed HPR topology comprises a group-type three-limb four-winding PF transformer, a series converter, and a shunt converter, as shown in Fig. 1a. The wiring scheme of the group-type three-limb four-winding PF transformer is shown in Fig. 1b. The three-limb four-winding PF transformer comprises a three-limb transformer core, medium-voltage, series, low-voltage, and parallel windings. The medium-voltage winding of the PF transformer is delta-connected to a 10 kV distribution power grid, the series winding is star-connected to the AC side of the series converter, the low-voltage winding is star-connected to form a 400 V low-voltage AC (LVAC) grid, and the parallel winding is star-connected to the AC side of the shunt PEC. The DC sides of the shunt PEC and the series converter are connected together to form a low-voltage DC (LVDC) port, as shown in Fig. 1c. Compared with the conventional PR topology based on multiple PEC modules, the proposed hybrid scheme has the following advantages:

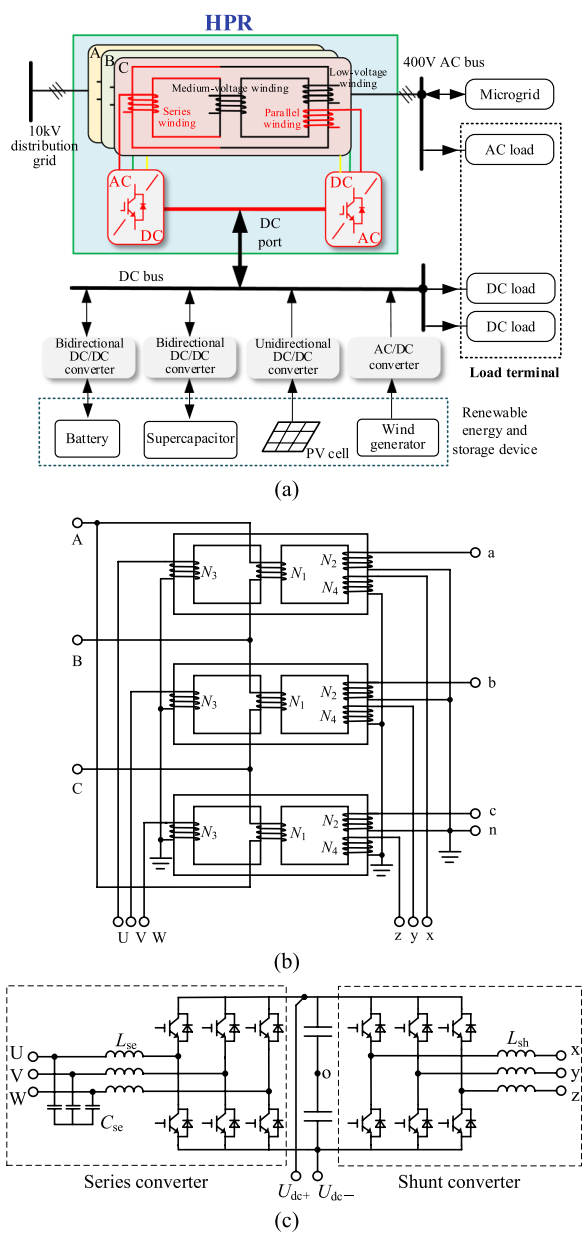

Fig. 1 Typology of the Proposed HPR. **a** Typology of hybrid power router (HPR); **b** Wiring scheme of group-type three-limb four-winding transformer; **c** Series and shunt PEC topologies

(1) Simple topology and control complexity. In the medium-voltage distribution grid scenario, only part of required power needs to be converted by the series and shunt PECs of the HPR, and generally, no multilevel or multistage cascaded typologies are required, leading to a simpler topology and control complexity.
(2) Low investment cost. With the PF transformer, which is low in price and mature in technology, only a few PEC modules are needed to realize active control. This significantly reduces the investment cost.
(3) Low operating loss. With the PF transformer, which has an operating efficiency of greater than 99%, the HPR has the advantage of high operating efficiency.
(4) High reliability. The reliability of the electromagnetic transformer is much higher than that of the PEC device. When a PEC module fails, only the winding bypass or open circuit scheme is required, without disconnecting the transformer's power supply.

3 Operating principle of HPR

3.1 Equivalent model of the PF transformer

The proposed HPR is modeled to reflect the coupling relationship between the PF transformer and the series and shunt PEC modules. Given the relatively mature modeling methods for series and shunt converters, which can be equivalent to controlled voltage and current sources, it mainly describes the modeling of the new PF transformer and its coupling relationship with the converters in this section. Considering the group-type transformer as an example, the proposed three-limb four-winding transformer is formed by adding the left limb, and series and parallel windings, as shown in Fig. 2. The voltage and current are denoted as v_1 and

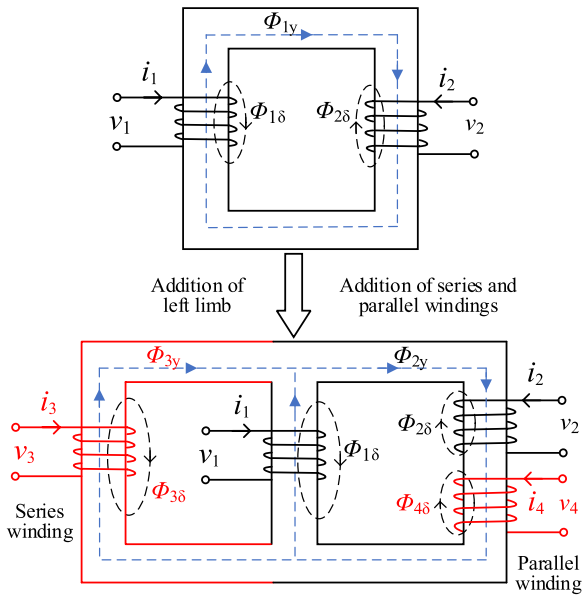

Fig. 2 Typology of the three-limb four-winding PF transformer

i_1 for the primary winding of the transformer y-phase (y=a, b, c), v_2 and i_2 for the secondary winding, v_3 and i_3 for the series winding, and v_4 and i_4 for the parallel winding, respectively. $\Phi_{1\delta}$, $\Phi_{2\delta}$, $\Phi_{3\delta}$, and $\Phi_{4\delta}$ denote the leakage fluxes of the primary, secondary, series, and parallel windings, respectively. Φ_{2y} and Φ_{3y} denote the magnetic fluxes of the two yokes. For simplicity, the mutual leakage fluxes among different windings are ignored. The reference directions of quantities, such as voltage, current, and magnetic flux, are shown in Fig. 2.

From the magnetic flux distribution shown in Fig. 2, the equivalent magnetic circuit (magnetic flux–magnetomotive force) model of the three-limb four-winding transformer can be obtained as shown in Fig. 3. S_{1L}, S_{2L}, and S_{3L} denote the magnetic resistances of the center, right, and left limb cores, respectively. S_{2y} and S_{3y} denote the magnetic resistances of the yokes, while $S_{1\delta}$–$S_{4\delta}$ denote the magnetic resistances of the leakage fluxes of the windings. F_i denotes the magnetomotive force of each winding. The total magnetic flux of each winding is equal to the sum of the main magnetic flux and leakage flux, as:

$$\begin{aligned}\Phi_{11}&=\Phi_{1\delta}+\Phi_{2y}-\Phi_{3y}\\ \Phi_{33}&=\Phi_{3y}+\Phi_{3\delta}\\ \Phi_{22}&=\Phi_{2y}+\Phi_{2\delta}\\ \Phi_{44}&=\Phi_{2y}+\Phi_{4\delta}\end{aligned} \tag{1}$$

The magnetomotive force of each winding is given by:

$$F_i = N_i i_i \tag{2}$$

where the subscript i (i=1, 2, 3, 4) represents the number of each winding, while N_1, N_2, N_3, and N_4 are the turns of the primary, secondary, series, and parallel windings, respectively.

According to Fig. 3 and based on Ohm's law of the magnetic circuit and the principle of node magnetomotive force balance, the magnetomotive force–magnetic resistance–magnetic flux relationship of the three-limb four-winding transformer can be expressed in matrix form as shown in (3).

$$\begin{bmatrix}F_1\\0\\F_2\\0\\F_3\\F_4\end{bmatrix}=\begin{bmatrix}S_{1\delta} & -S_{1\delta} & 0 & S_{1\delta} & 0 & 0\\ -S_{1\delta} & S_{1\delta}+S_{2\delta}+S_{4\delta}+S_{1L}+S_{2L}+S_{2y} & -S_{2\delta} & -S_{1\delta}-S_{1L} & 0 & -S_{4\delta}\\ 0 & -S_{2\delta} & S_{2\delta} & 0 & 0 & 0\\ S_{1\delta} & -S_{1\delta}-S_{1L} & 0 & S_{1\delta}+S_{3\delta}+S_{1L}+S_{3L}+S_{3y} & -S_{3\delta} & 0\\ 0 & 0 & 0 & -S_{3\delta} & S_{3\delta} & 0\\ 0 & -S_{4\delta} & 0 & 0 & 0 & S_{4\delta}\end{bmatrix}\begin{bmatrix}\Phi_{11}\\\Phi_{2y}\\\Phi_{22}\\\Phi_{3y}\\\Phi_{33}\\\Phi_{44}\end{bmatrix} \tag{3}$$

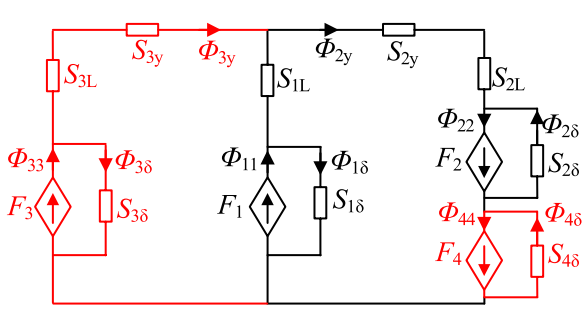

Fig. 3 Equivalent magnetic circuit model of the three-limb four-winding PF transformer

Equation (3) can also be expressed in simple terms as:

$$\boldsymbol{F}=\boldsymbol{S\Phi} \tag{4}$$

To deduce the equivalent circuit of the PF transformer, Eq. (3) can be further transformed with the magnetomotive force of each winding expressed in matrix form as:

$$\boldsymbol{F}=N\boldsymbol{I}' \tag{5}$$

where I' denotes the winding current matrix when the turns N_1, N_2, N_3, and N_4 are normalized to the number of turn N.

According to Faraday's law of electromagnetic induction, the relationship between the four-winding transformer port voltage $\boldsymbol{V}'$ and the magnetic flux $\boldsymbol{\Phi}$ is:

$$\boldsymbol{V}' = N\frac{\mathrm{d}\Phi}{\mathrm{d}t} = j\omega N\boldsymbol{\Phi} \tag{6}$$

Substituting (5) and (6) into (4) yields:

$$N\boldsymbol{I}' = \boldsymbol{S}\frac{\boldsymbol{V}'}{j\omega N} \tag{7}$$

Equation (7) can be further transformed into:

$$\boldsymbol{I}' = \frac{\boldsymbol{S}}{j\omega N^2}\boldsymbol{V}' \tag{8}$$

Equation (8) is the nodal voltage equation of the three-limb four-winding transformer. The inductance of each magnetic circuit is defined as:

$$L = \frac{N^2}{S} \tag{9}$$

$$\begin{bmatrix} i_1' \\ 0 \\ i_2' \\ 0 \\ i_3' \\ i_4' \end{bmatrix} = \begin{bmatrix} \frac{1}{Z_{1\delta}} & -\frac{1}{Z_{1\delta}} & 0 & \frac{1}{Z_{1\delta}} & 0 & 0 \\ -\frac{1}{Z_{1\delta}} & \frac{1}{Z_{1\delta}}+\frac{1}{Z_{2\delta}}+\frac{1}{Z_{4\delta}}+\frac{1}{Z_{1L}}+\frac{1}{Z_{2L}}+\frac{1}{Z_{2y}} & -\frac{1}{Z_{2\delta}} & -\frac{1}{Z_{1\delta}}-\frac{1}{Z_{1L}} & 0 & -\frac{1}{Z_{4\delta}} \\ 0 & -\frac{1}{Z_{2\delta}} & \frac{1}{Z_{2\delta}} & 0 & 0 & 0 \\ \frac{1}{Z_{1\delta}} & -\frac{1}{Z_{1\delta}}-\frac{1}{Z_{1L}} & 0 & \frac{1}{Z_{1\delta}}+\frac{1}{Z_{3\delta}}+\frac{1}{Z_{1L}}+\frac{1}{Z_{3L}}+\frac{1}{Z_{3y}} & -\frac{1}{Z_{3\delta}} & 0 \\ 0 & 0 & 0 & -\frac{1}{Z_{3\delta}} & \frac{1}{Z_{3\delta}} & 0 \\ 0 & -\frac{1}{Z_{4\delta}} & 0 & 0 & 0 & \frac{1}{Z_{4\delta}} \end{bmatrix} \begin{bmatrix} v_1' \\ v_{2y}' \\ v_2' \\ v_{3y}' \\ v_3' \\ v_4' \end{bmatrix} \tag{10}$$

From (8) and (9), the equivalent circuit model of the three-limb four-winding transformer can be obtained as shown in (10), where $Z = j\omega L$. From (10) and Kirchhoff's voltage and current laws, the equivalent circuit of the three-limb four-winding transformer can be obtained as shown in Fig. 4a. With consideration of the normalization turn N, the equivalent circuit can be further transferred to Fig. 4b. It is noted that the equivalent circuit model of the three-limb four-winding transformer is a series–parallel combination relationship in which the electrical circuit and the magnetic circuit are coupled. Given the small magnetic resistance of the core limb and yoke (i.e., the large excitation impedance corresponding to the main electromotive force of each winding) [24], if the influence of the excitation branches are ignored, i.e., branches Z_{1L}, Z_{2L}, Z_{3L}, Z_{3y}, and Z_{2y} in Fig. 4 are disconnected as shown in Fig. 4c, the winding voltages v_1, v_3 and v_2 (v_4) are in series, while v_2 and v_4 are in parallel. Therefore, the following conclusions can be drawn from the equivalent magnetic circuit model in Fig. 3 and the equivalent electrical circuit model in Fig. 4:

(1) The primary winding N_1 and series winding N_3 of the new PF transformer are in series, and thus the amplitude and phase of the low-voltage side voltage v_2 can be adjusted when the amplitude and phase of the series winding voltage v_3 are regulated. For a voltage dip or distortion because of an MVAC distribution grid fault, the compensation by the series winding voltage v_3 can ensure that the low-voltage side voltage v_2 is unaffected, thereby improving power supply reliability.
(2) The low-voltage winding N_2 and parallel winding N_4 of the new PF transformer are in parallel, and thus the amplitude and phase of the low-voltage side current i_2 can be adjusted when the amplitude and phase of the parallel winding current i_4 are regulated to realize the active power control of the LVAC and LVDC ports. In addition, in the case of reactive power, harmonic and unbalanced power quality problems in the LVAC power grid, the compensation by the parallel winding current i_4 can ensure that the current and voltage of the MVAC port are in phase and the waveforms are sinusoidal, thereby improving power quality.

3.2 Control principle of HPR

From the modeling analysis in Sect. 3.1, the active voltage and current control of the HPR can be realized by adjusting the voltage and current of the series/parallel windings of the new PF transformer. Therefore, the basic control ideas of the HPR are as follows:

(1) In steady-state conditions, the active power exchanged between LVAC and LVDC grids, and LVAC grid current quality, are controlled by the shunt converter, whereas the amplitude and phase of the LVAC grid voltage are controlled by the series converter.
(2) In fault conditions of the MVAC distribution grid, the series converter outputs the compensation voltage to ensure that the LVAC grid voltage is unaffected.

In grid steady-state conditions, the power exchange among the MVAC grid and the LVAC and LVDC grids

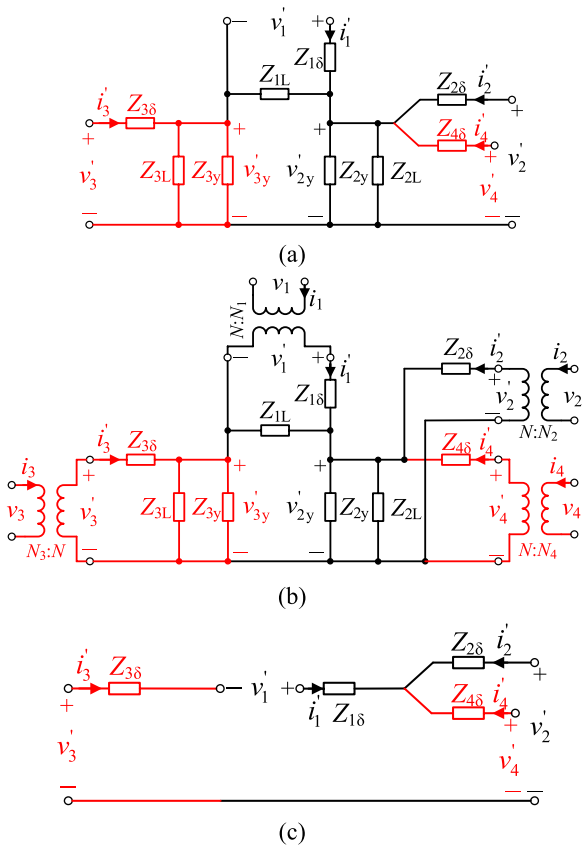

Fig. 4 Equivalent electrical circuits of the new three-limb four-winding PF transformer. **a** Equivalent circuit after normalization to number of turn *N*; **b** Equivalent circuit considering the turn ratio of windings; **c** Equivalent circuit without considering the influence of the excitation branch

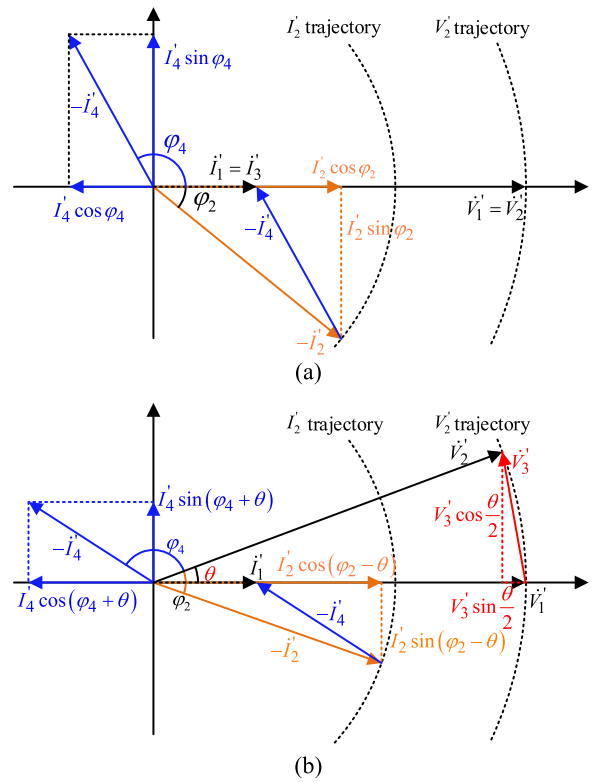

Fig. 5 Voltage–current phasor diagram of HPR in steady-state conditions. **a** Without considering series winding voltage regulation; **b** With considering series winding voltage regulation

is controlled by the new PF transformer and the series/shunt PECs. When the capacity is sufficient, there is no power transmitted by the series converter, and the normalized MVAC grid voltage (v_1') is equal to the LVAC grid voltage (v_2') in terms of amplitude and phase.

Figure 5a depicts the voltage–current phasor diagram of the HPR, and Fig. 6 depicts the power flow between the HPR ports. The relationships of the active and reactive power at each port are given as:

$$\begin{cases} P_{\mathrm{MVac}} + P_{\mathrm{sh}} = P_{\mathrm{LVac}} \\ Q_{\mathrm{sh}} = Q_{\mathrm{LVac}},\ Q_{\mathrm{MVac}} = 0 \end{cases} \tag{11}$$

where P_{MVac} and Q_{MVac} denote the active and reactive power involved in the interaction between the MVAC port of the HPR and the MVAC grid, respectively, with $P_{\mathrm{MVac}} > 0$ indicating power being absorbed from the grid and $P_{\mathrm{MVac}} < 0$ indicating power being fed back to the grid. P_{sh} and Q_{sh} denote the active and reactive power involved in the LVAC and LVDC grids interaction of the shunt converter, respectively, with $P_{\mathrm{sh}} > 0$ indicating active power being transmitted from the LVDC grid to the LVAC grid and vice versa for $P_{\mathrm{sh}} < 0$. P_{LVac} and Q_{LVac} denote the active and reactive power consumed by the LVAC load, respectively, with $Q_{\mathrm{LVac}} > 0$ indicating inductive reactive power and $Q_{\mathrm{LVac}} < 0$ indicating capacitive reactive power. At this time, the output voltage of the series converter and the output current of the shunt converter satisfy the following relationship:

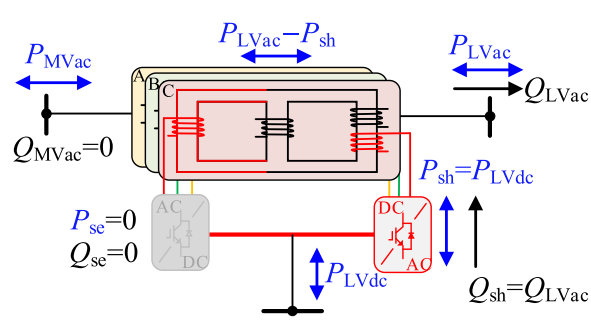

Fig. 6 Power flow between the HPR ports in steady-state conditions (without series winding voltage regulation)

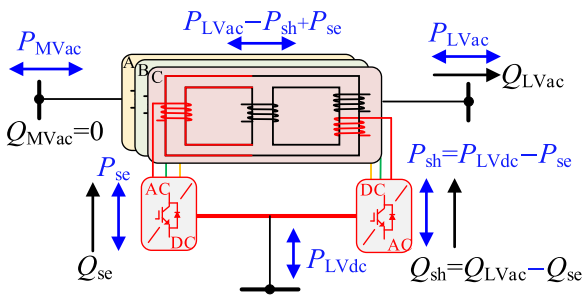

Fig. 7 Power flow between the HPR ports in steady-state or fault conditions (with series winding voltage regulation)

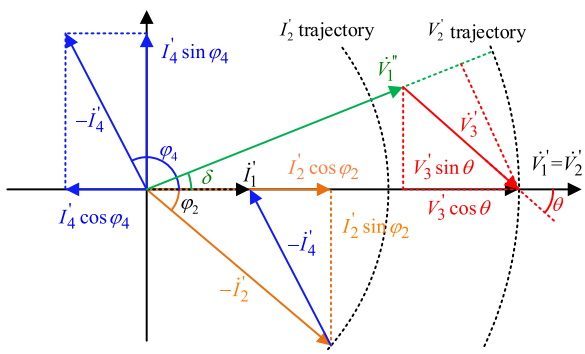

Fig. 8 Voltage–current phasor diagram of HPR in MVAC grid fault conditions (with series winding voltage regulation)

$$\begin{cases} \dot{V}_3' = 0 \\ I_1' = I_2' \cos\varphi_2 + I_4' \cos\varphi_4 \\ 0 = I_2' \sin\varphi_2 + I_4' \sin\varphi_4 \end{cases} \tag{12}$$

In addition to compensating for the reactive power of the load with the shunt converter, the series converter can be used to regulate the phase shift between the LVAC and MVAC grid voltages to realize the reactive power regulation function of the series converter, as shown in Fig. 5b, and the power flows between the HPR ports are shown in Fig. 7. In this case, the relationships of the active and reactive power at each port are given as:

$$\begin{cases} P_{MVac} + P_{LVdc} = P_{LVac},\ P_{sh} = P_{LVdc} - P_{se} \\ Q_{sh} + Q_{se} = Q_{LVac},\ Q_{MVac} = 0 \end{cases} \tag{13}$$

where $P_{LVdc}=P_{LVdc,DG}+P_{LVdc,ESS}-P_{LVdc,Ld}$ denotes the active power transmitted by the LVDC port, $P_{LVdc,DG}$ denotes the power supplied by the renewable energy, $P_{LVdc,ESS}$ denotes the power supplied or absorbed by the storage energy, and $P_{LVdc,Ld}$ denotes the power consumed by the LVDC load. P_{se} and Q_{se} denote the active and reactive power controlled by the series converter, respectively.

From Fig. 5b and (13), the reactive power of the LVAC load can be redistributed between the series and shunt converters in any proportion. The series converter can absorb active power while supplying reactive power, while at this time, the output voltage of the series converter and the output current of the shunt converter satisfy the following relationship:

$$\begin{cases} V_3' \sin(0.5\theta) = V_1' - V_2' \cos\theta \\ V_3' \cos(0.5\theta) = V_2' \sin\theta \\ I_1' = I_2' \cos(\varphi_2 - \theta) + I_4' \cos(\varphi_4 + \theta) \\ 0 = I_2' \sin(\varphi_2 - \theta) + I_4' \sin(\varphi_4 + \theta) \end{cases} \tag{14}$$

During grid faults, the LVAC grid voltage can be kept in the rated steady-state value by adjusting the voltage injected by the series winding (v_3'). The power flows among HPR ports are shown in Fig. 7, and the voltage–current phasor diagram of the HPR is presented in Fig. 8. At this time, the output voltage of the series converter satisfies the following relationship:

$$\begin{cases} V_3' \cos\theta = V_1' - V_1'' \cos\delta \\ V_3' \sin\theta = V_1'' \sin\delta \end{cases} \tag{15}$$

where V_1'' denotes the magnitude of the primary winding voltage after the sudden change of the MVAC grid voltage, while δ denotes the phase jump angle.

4 Control strategy of HPR

As the power supply equipment of a regional distribution grid, a PR should ensure the basic control of the voltage/current conversion, and power transfer of the PEC modules. In addition, a PR should coordinate the operational control of each port by comprehensively considering the characteristics of the source-grid-load-storage device connected at each port. Also, a PR should flexibly change the operational mode to adapt to different operating environments when the external power grid fails, or the power grid is under maintenance.

In this paper, a hierarchical control strategy including the system-level and converter-level is established to control the power/voltage of each port of the HPR in real time, as shown in Fig. 9. In Fig. 9, $v_{MVac,abc}$ and $i_{MVac,abc}$ are the voltage and current at the MVAC port, $v_{LVac,abc}$ and $i_{LVac,abc}$ are the voltage and current at the LVAC port, while $v_{se,abc}$, $i_{se,abc}$ and $v_{sh,abc}$, $i_{sh,abc}$ are the voltage and current at the AC side of the series PEC and shunt PEC, respectively. v_{LVdc} is the DC bus voltage of the LVDC grid. In the sequence decomposition part, x denotes the three-phase voltage or current, and q is a phase-shift operator in the time-domain. This obtains the quadrature-phase waveform (90-degrees lag) of the original in-phase waveform. In the PLL part, θ^+ is the positive phase angle of the

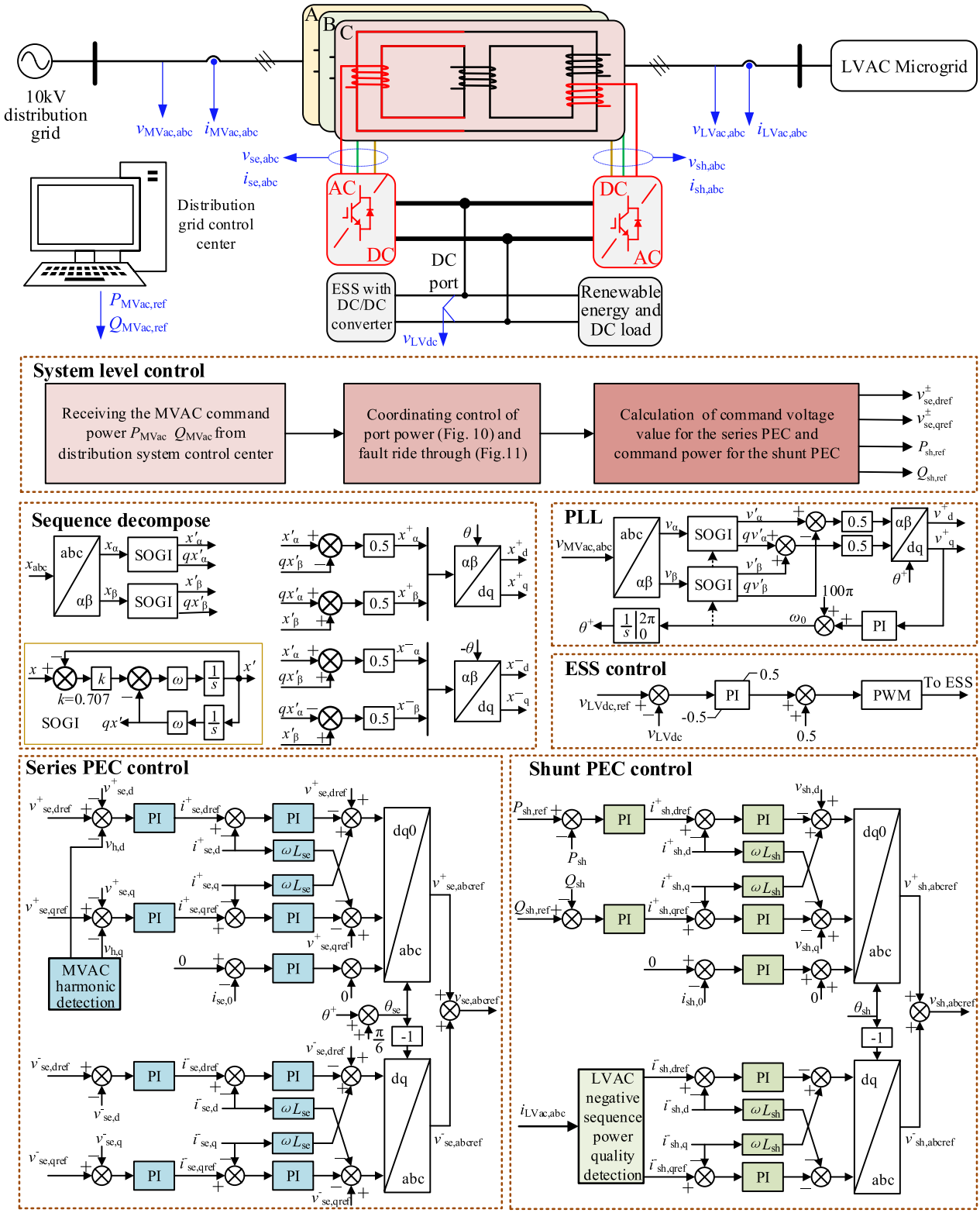

Fig. 9 Overall control block diagram of the proposed HPR

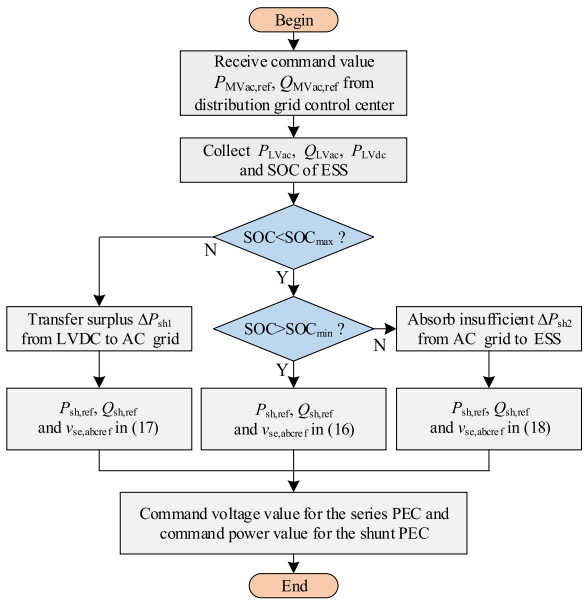

Fig. 10 System-level coordinated control strategy of the HPR in steady-state conditions

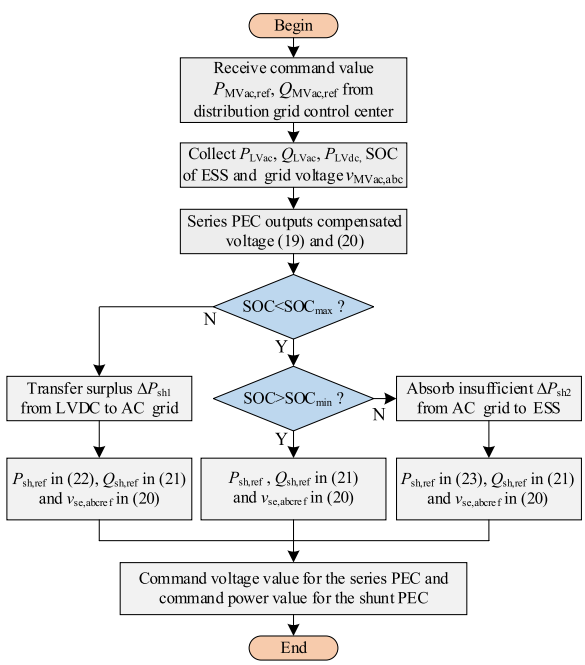

Fig. 11 System-level coordinated control strategy of the HPR in grid fault conditions

MVAC grid voltage. θ_{se} and θ_{sh} are the respective phase angles for the series PEC and shunt PEC. The superscripts '+' and '−' indicate positive and negative variables of voltage and current in the dq-frame, respectively.

For system-level control, the power/voltage command of each port is obtained through the interaction with the power distribution grid control center to realize the coordinated control of the operational mode, fault isolation, and fault ride-through. When the system-level control layer receives a scheduling instruction from the distribution grid control center, the working condition instructions are issued to the HPR controller according to the collected port information and HPR status. Even if there is no scheduling instruction, the appropriate working conditions can be selected based on the current working state of the HPR controller. The system-level coordinated control strategies in steady-state and grid fault conditions are shown in Figs. 10 and 11, respectively.

In steady-state conditions, the system-level control layer receives a scheduling instruction $P_{MVac,ref}$, $Q_{MVac,ref}$ and $v_{se,abcref}$ from the distribution grid control center, and collects each port status of the HPR, including P_{LVac}, Q_{LVac}, P_{LVdc} and the state-of charge (SOC) of the ESS. If the SOC of the ESS is within the normal range [SOC$_{min}$, SOC$_{max}$], the ESS maintains the DC bus voltage of the LVDC grid, and the shunt PEC provides the active and reactive power ($P_{sh,ref}$, $Q_{sh,ref}$) supplement or absorption when a power compensation is needed from the distribution grid control center, shown as:

$$\begin{cases} P_{sh,ref} = P_{MVac,ref} - P_{LVac} \\ Q_{sh,ref} = Q_{MVac,ref} - Q_{LVac} \\ v_{se,abcref} = 0 \end{cases} \tag{16}$$

It should be noted that there is no need to output the compensated voltage $v_{se,abc}$ for the series PEC in steady-state conditions, i.e., $v_{se,abcref}=0$. If the SOC of the ESS is out of the normal range, the shunt PEC has to revise the command value to maintain the DC bus voltage. If the SOC of the ESS is larger than SOC$_{max}$, it means too much power for the LVDC grid. The shunt PEC will transfer surplus power ΔP_{sh1} from the LVDC to the AC grid. Then, the updated active and reactive power command values can be expressed as:

$$\begin{cases} P_{sh,ref} = P_{MVac,ref} - P_{LVac} + \Delta P_{sh1} \\ Q_{sh,ref} = Q_{MVac,ref} - Q_{LVac} \\ v_{se,abcref} = 0 \end{cases} \tag{17}$$

If the SOC of the ESS is smaller than SOC$_{min}$, the shunt PEC has to absorb insufficient power ΔP_{sh2} from AC grid for maintaining the DC bus voltage. Then, the active power command values can be revised as:

$$P_{sh,ref} = P_{MVac,ref} - P_{LVac} - \Delta P_{sh2} \tag{18}$$

In grid fault conditions, the system-level control layer needs to prioritize the voltage compensation function. In order to avoid the phase angle jump at the LVAC grid during grid faults, the series PEC has to compensate the sag/swell voltage so that the LVAC voltage is well compensated with respect to the pre-sag/swell voltage. Because of the Dyn11 connection of the 10 kV / 400 V PF transformer, there exists a π/6-degree shift between the MVAC and LVAC sides. Then, the desired LVAC grid voltage $v_{\mathrm{LVac,abcref}}$ can be expressed as:

$$\begin{cases} v_{\mathrm{LVac,aref}} = V_{\mathrm{LVac,N}} \sin\left(\theta^{+} + \pi/6\right) \\ v_{\mathrm{LVac,bref}} = V_{\mathrm{LVac,N}} \sin\left(\theta^{+} + \pi/6 - 2\pi/3\right) \\ v_{\mathrm{LVac,cref}} = V_{\mathrm{LVac,N}} \sin\left(\theta^{+} + \pi/6 + 2\pi/3\right) \end{cases} \tag{19}$$

where $V_{\mathrm{LVac,N}}$ is the nominal amplitude of the LVAC grid voltage.

Then, to maintain the LVAC voltage at a nominal value and achieve phase angle correction, the series PEC voltage references $v_{\mathrm{se,abcref}}$ can be generated as:

$$\begin{cases} v_{\mathrm{se,aref}} = \frac{N_3}{N_2} v_{\mathrm{LVac,aref}} - \frac{N_3}{N_1} v_{\mathrm{MVac,ab}} \\ v_{\mathrm{se,bref}} = \dfrac{N_3}{N_2} v_{\mathrm{LVac,bref}} - \dfrac{N_3}{N_1} v_{\mathrm{MVac,bc}} \\ v_{\mathrm{se,cref}} = \dfrac{N_3}{N_2} v_{\mathrm{LVac,cref}} - \dfrac{N_3}{N_1} v_{\mathrm{MVac,ca}} \end{cases} \tag{20}$$

where N_1, N_2, N_3, and N_4 are the turns of the primary, secondary, series, and parallel windings, respectively. $v_{\mathrm{MVac,ab}}$, $v_{\mathrm{MVac,bc}}$ and $v_{\mathrm{MVac,ca}}$ are the line voltages of the MVAC grid. After the sequence decomposition and abc/dq transformation, the d-axis and q-axis components can be respectively derived as $v^{+}_{\mathrm{se,dref}}/v^{+}_{\mathrm{se,qref}}$, and $v^{-}_{\mathrm{se,dref}}/v^{-}_{\mathrm{se,qref}}$.

To avoid overcurrent at the MVAC port during a grid fault, the transferred power $P_{\mathrm{MVac,ref}}$, $Q_{\mathrm{MVac,ref}}$ will be revised with respect to the severity of the grid fault. We define $D = V_{\mathrm{MVac}} / V_{\mathrm{MVac,N}} \in [0, 1]$ as a voltage dip factor representing the severity of the grid fault, where V_{MVac} and $V_{\mathrm{MVac,N}}$ are the actual and nominal phase voltage amplitudes of the MVAC grid, respectively. Then, the active and reactive power ($P_{\mathrm{sh,ref}}$, $Q_{\mathrm{sh,ref}}$) supplement or absorption by the shunt PEC in (16)–(19) are updated as:

$$\begin{cases} P_{\mathrm{sh,ref}} = DP_{\mathrm{MVac,ref}} + P_{\mathrm{se}} - P_{\mathrm{LVac}} \\ Q_{\mathrm{sh,ref}} = DQ_{\mathrm{MVac,ref}} + Q_{\mathrm{se}} - Q_{\mathrm{LVac}} \end{cases} \tag{21}$$

$$P_{\mathrm{sh,ref}} = DP_{\mathrm{MVac,ref}} + P_{\mathrm{se}} - P_{\mathrm{LVac}} + \Delta P_{\mathrm{sh1}} \tag{22}$$

$$P_{\mathrm{sh,ref}} = DP_{\mathrm{MVac,ref}} + P_{\mathrm{se}} - P_{\mathrm{LVac}} - \Delta P_{\mathrm{sh2}} \tag{23}$$

where $P_{\mathrm{se}} = (1-D)P_{\mathrm{MVac,ref}}$ and $Q_{\mathrm{se}} = (1-D)Q_{\mathrm{MVac,ref}}$. In addition, in the case of severe short circuit faults or prolonged voltage sags which exceed the system capacity, the HPR needs to cooperate with the relay protection of the MVAC grid to convert to islanded mode. In this case, load-shedding may have to be considered to maintain healthy operation of the ESS.

For the converter-level control, the dual closed-loop control method under positive and negative dq0-frame is adopted [25]. The outer loop of the series converter calculates the current reference value by tracking the required injected series voltage, and the outer loop of the shunt converter calculates the current reference value based on the active and reactive power tracking. The inner loops of the series and shunt converters adopt feedforward decoupling current control. It is noted that either a proportional integral (PI) or proportional integral resonance (PIR) regulator can be used for the outer loop regulator (OLR) and the inter loop regulator (ILR) to precisely track the reference values, whereas the PI is used for the OLR and ILR in this paper. The second order generalized integrator (SOGI) method for decomposing the sequences of voltage and current signals is implemented here [26], as shown in Fig. 9. Also, the SOGI-based phase-locked loop (SOGI-PLL) [26] is used to provide an effective solution for grid synchronization in grid asymmetric faulty conditions. Finally, sinusoidal pulse width modulation (SPWM) technology is used to generate the switching signals for the switches of the series and shunt converters.

The function of the ESS with a DC/DC converter in the proposed HPR is to maintain the DC bus voltage of the LVDC grid [25, 27, 28], and to provide the active power supplement or absorption when a power compensation is needed for the power fluctuation in the proposed HPR. Since the LVDC DC bus voltage is controlled by the ESS with the bidirectional DC/DC converter, the shunt

Table 1 Simulation parameters of HPR

Parameter	Value
MVAC line-to-line voltage v_{MVac}/kV	10
LVAC line-to-line voltage v_{LVac}/V	400
LVDC voltage v_{LVdc}/V	1,500
Rated capacity of MVAC port	1MVA
Rated capacity of LVAC port	1MVA
Rated capacity of shunt PEC	1MVA
Rated capacity of series PEC	1MVA
Transformer turn ratio N_1:N_2:N_3:N_4	10000:231:462:462
Shunt PEC filter inductance L_{sh}/mH	1
Shunt PEC filter capacitance C_{sh}/μF	2,000
Series PEC filter inductance L_{se}/mH	1
Series PEC filter capacitance C_{se}/μF	2,000
DC bus capacitance C_{dc}/mF	20,000
Switching frequency of PECs f_{sw}/kHz	10
Grid frequency f_{s}/Hz	50

converter can operate in active and reactive power control mode and the series converter in voltage control mode. The ESS control scheme with DC/DC converter is also shown in Fig. 9. The voltage loop is formed by comparing the real-time LVDC voltage v_{LVdc} with the reference LVDC voltage $v_{\mathrm{LVdc,ref}}$ before feeding into the PI regulator, whose output is then sent to the pulse width modulation (PWM) generator to generate the switching signals.

5 Simulation results

The distribution grid/microgrid shown in Fig. 1 is built on the MATLAB/Simulink + Plecs platform to verify the feasibility of the proposed HPR. The main parameters of the HPR are shown in Table 1. Among them, the LVAC active and reactive load is simulated with a resistor and an inductor, the storage energy is connected to the LVDC bus through the bidirectional Boost converter, and the DC load is resistive.

In the MVAC grid steady-state conditions, the simulation settings are as follows:

- From 1.0 to 1.1 s, the active and reactive power of the LVAC grid are 400 kW + j300 kVar. At this time, the shunt PEC only compensates for the reactive power of the LVAC grid and the transmitted active power is 0. As the MVAC grid voltage is normal, the output voltage of the series PEC is also 0.
- From 1.1 to 1.2 s, the active and reactive power of the LVAC grid suddenly increase by 400 kW + j300 kVar. At this time, the shunt PEC still only compensates for the reactive power of the LVAC grid, and the transmitted active power by the shunt PEC is 0.
- From 1.2 to 1.3 s, the LVDC grid transmits 300 kW active power to the LVAC grid through the shunt PEC.

Figures 12 and 13 show the dynamic simulation results of the power flows among the HPR ports. As shown in Fig. 12c, d, the LVAC grid voltage is always at the rated value under the sudden change of LVAC load. After the reactive power compensation by the shunt PEC, as shown in Fig. 12h, the voltage and current of the MVAC port are in phase, indicating only active power is provided by MVAC grid, as shown in Fig. 12b. Because no compensation voltage is required from the series PEC in steady-state, the active and reactive power transmitted by the series PEC remain at 0, as shown in Fig. 13. Therefore, the active power transmitted by the shunt PEC can be regulated in steady-state to adjust the power control between the LVAC and LVDC grids, and the power quality of the LVAC grid can be compensated by the HPR, ensuring that the voltage and current of the MVAC port are in phase with sinusoidal waveforms.

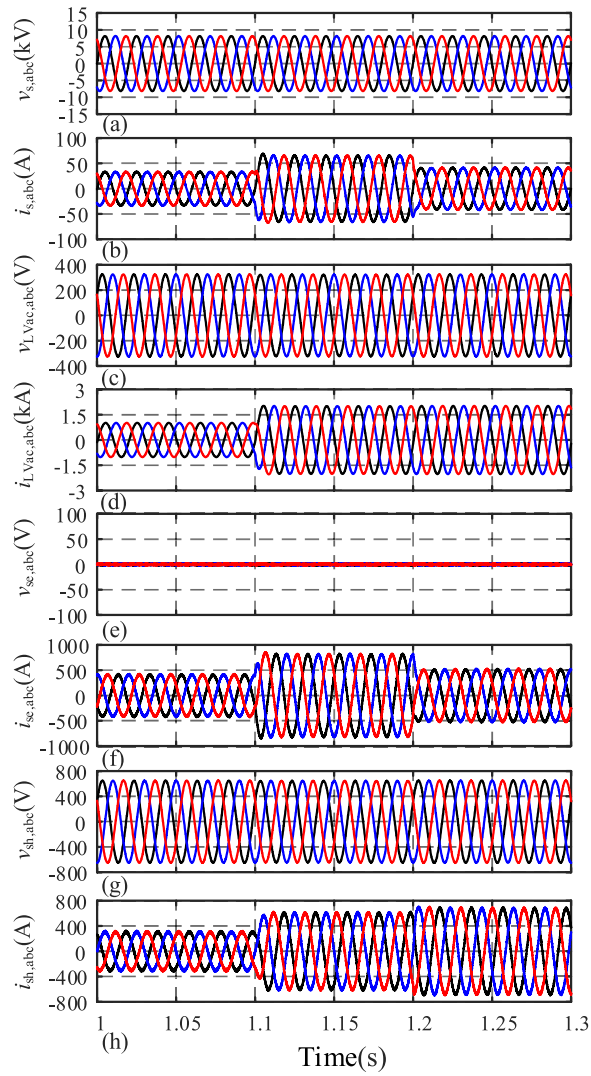

Fig. 12 Dynamic simulation waveforms of voltage and current of HPR in steady-state conditions

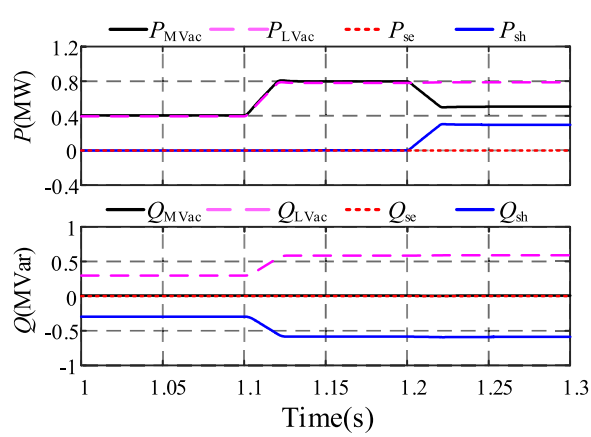

Fig. 13 Dynamic simulation waveforms of power flow among the HPR ports in steady-state conditions

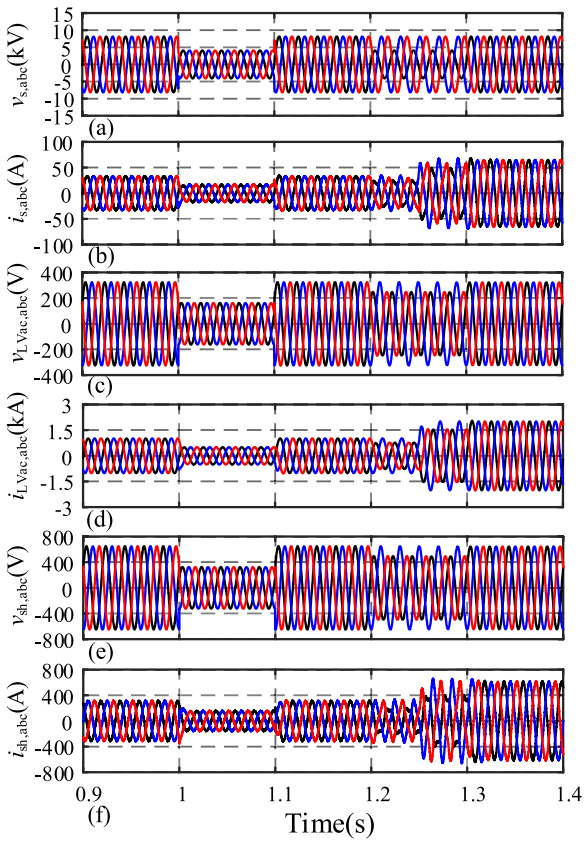

Fig. 14 Dynamic simulation waveforms of the conventional transformer in an MVAC grid fault

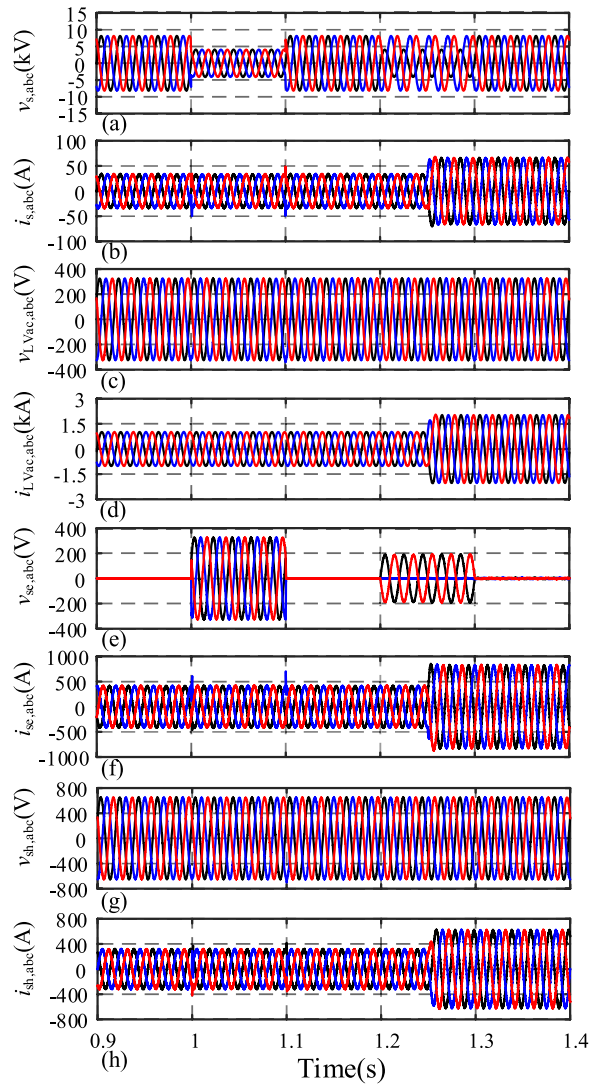

Fig. 15 Dynamic simulation waveforms of the proposed HPR under MVAC grid fault conditions

In the MVAC grid fault conditions, the simulation settings are as follows: from 1.0 to 1.1 s, the three-phase voltage of the MVAC grid drops symmetrically by 50%; from 1.2 to 1.3 s, the phase A voltage of the MVAC grid drops by 50%; and at 1.25 s, the active and reactive powers of the LVAC grid increase by 400 kW + j300 kVar.

Figure 14 shows the dynamic simulation results of a conventional transformer in grid fault conditions. Because the conventional transformer has no series voltage compensation correction function, a symmetrical or asymmetrical voltage dip occurs in the LVAC grid during a symmetrical or asymmetrical MVAC grid fault, as shown in Fig. 14a, c. For the asymmetric LVAC voltage, the output three-phase current of the shunt PEC without the fault ride-through function will be severely distorted (see the current waveforms during 1.2–1.3 s in Fig. 14f), and the current at the MVAC port will also be distorted. Therefore, the fault isolation and voltage support capability cannot be achieved using the conventional transformer during the MVAC grid fault.

Figure 15 shows the dynamic simulation results of the HPR in MVAC grid fault conditions. During a symmetrical or asymmetrical voltage dip on the MVAC grid, as shown in Fig. 15a, the series PEC can be controlled to inject a support voltage to ensure that the LVAC grid voltage is always at the rated value and unaffected by the MVAC grid voltage disturbance, as shown in Fig. 15c, e, thereby ensuring high-quality power supply for LVAC and LVDC users and renewable energy power generation equipment. During a symmetric or asymmetric voltage dip of the MVAC grid, the power at each port of HPR satisfies $P_{MVac}+P_{sh}+P_{se}=P_{LVac}$, $Q_{sh}+Q_{se}=Q_{LVac}$, and $Q_{MVac}=0$, as shown in Fig. 16. In conclusion, the proposed HPR can realize fault isolation between MVAC and LVAC grids with the active voltage support of the series winding, thereby improving the power supply reliability.

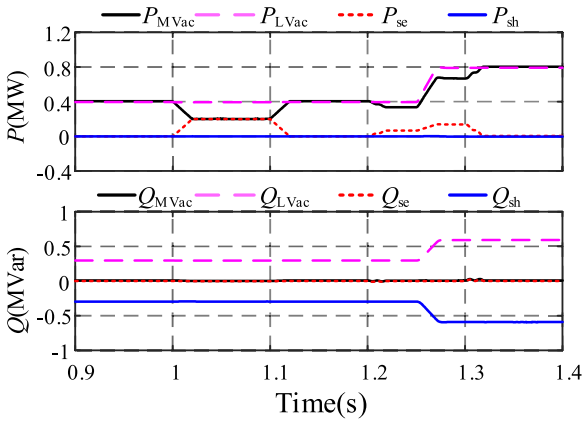

Fig. 16 Dynamic simulation waveforms of power flow among the HPR ports in MVAC grid fault conditions

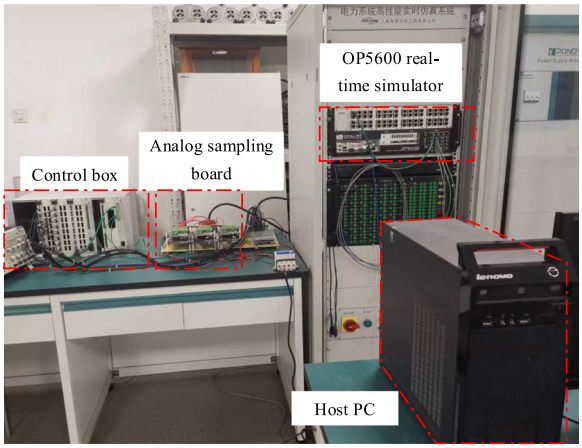

Fig. 17 RTLAB-Based CHIL platform

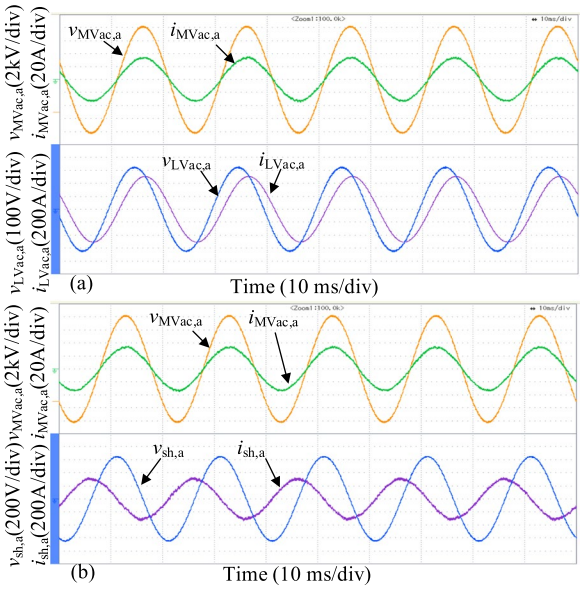

Fig. 18 Voltage and current waveforms at each HPR port in steady-state condition. **a** Phase A voltage and current at MVAC and LVAC ports; **b** Phase A voltage and current at MVAC and parallel winding ports

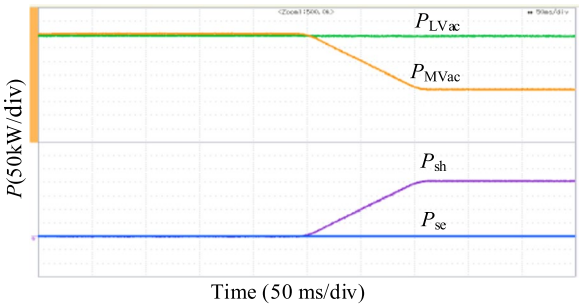

Fig. 19 Results of port power change of the proposed HPR under dynamic operation

6 CHIL and down-scale experimental test results

6.1 CHIL test results

An RTLAB-based CHIL is built to further validate the correctness of the proposed HPR typology and theoretical analysis. As shown in Fig. 17, the HPR and grids are modeled in the OP5600 real-time simulator. The control system of the HPR is implemented in a DSP + FPGA-based control box, with the DSP (TMS320F28335) used for the control algorithm implementation, and the FPGA (EP3C25E144I7N) for the SPWM and optical fiber communication. The control box is connected to RT-LAB through the signal conversion module for optical fiber communication. The CHIL parameters are consistent with the simulation parameters.

Figure 18 shows the waveforms of the phase A voltage and current at each HPR port in grid steady-state conditions. The active and reactive power of the LVAC grid are 400 kW + j300 kVar. At this time, the LVAC current lags behind the voltage, as shown in Fig. 18a. The shunt PEC only compensates for the reactive power of the LVAC grid, so the transmitted active power is 0, as shown in Fig. 18b, while the MVAC voltage and current are in phase. Figure 19 shows the dynamic waveforms of power change of the HPR ports in steady-state conditions. The shunt PEC outputs reactive power and linearly increases the output active power by 200 kW

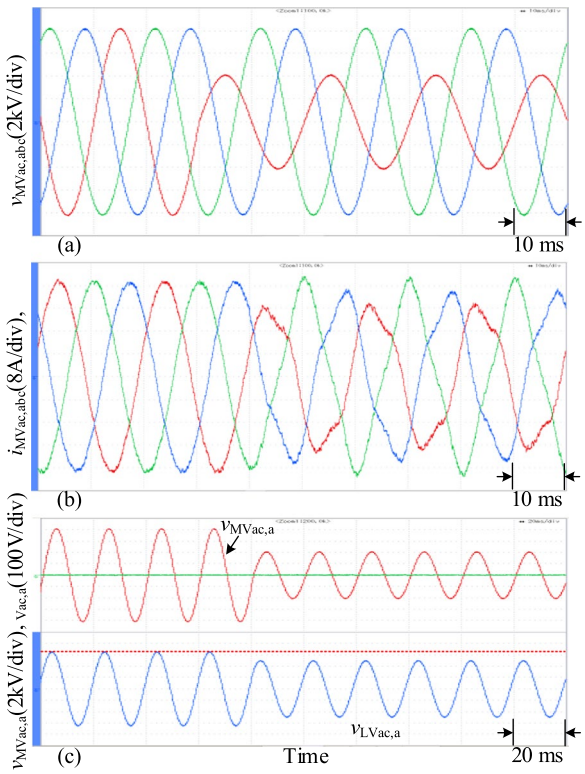

Fig. 20 Results of the conventional transformer in an MVAC grid asymmetrical fault condition. **a** three-phase MVAC grid voltage; **b** three-phase MVAC current; **c** Phase A voltages at MVAC, series winding, and LVAC

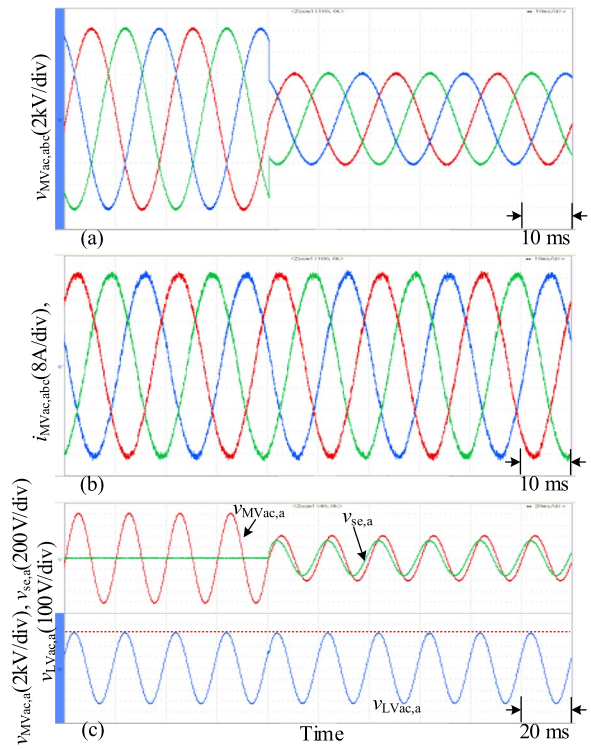

Fig. 21 Results of voltage support of the proposed HPR in an MVAC grid symmetrical fault condition. a three-phase MVAC grid voltage; **b** three-phase MVAC current; **c** Phase A voltages at MVAC port, series winding, and LVAC port

within 0.1 s. From Fig. 19, it can be concluded that the power transmitted by the HPR ports can be regulated by the shunt PEC module.

Figure 20 shows the CHIL results of the conventional transformer in MVAC grid asymmetrical fault conditions. The active and reactive powers of the LVAC grid maintain at 400 kW + j300 kVar, and the reactive power is compensated by the shunt PEC. Because the conventional transformer has no series voltage compensation correction function, an asymmetrical voltage dip occurs in the LVAC grid in the case of a MVAC grid asymmetrical fault, as shown in Fig. 20c. In addition, if the conventional PEC is not configured with the negative-sequence control loop and fault ride-through function, the current at the MVAC port is severely distorted because of the asymmetrical fault, as shown in Fig. 20b. Therefore, the voltage support capability cannot be achieved using a conventional transformer.

Figures 21 and 22 show the dynamic results of the HPR under MVAC grid symmetrical and asymmetrical fault conditions, respectively. When the voltage of the MVAC grid drops by 50%, the series PEC can be controlled to inject a support voltage to ensure that the LVAC grid voltage remains at the rated value and is unaffected by the MVAC grid disturbance, as shown in Figs. 21 and 22. Therefore, the fault isolation and voltage support capability can be well realized using the proposed HPR during the symmetrical and asymmetrical grid faults.

To further verify the disturbance/fault isolation performance of the HPR, the MVAC grid voltage is set to contain 0.1 pu 5th and 0.05 pu 7th harmonics. As shown in Fig. 23, the MVAC grid voltage is severely distorted. After the voltage correction by the series PEC, the LVAC voltage maintains a sinusoidal waveform, as shown in Fig. 23b. The CHIL results of these two abnormal conditions agree with the theoretical analysis and simulation results, so the active voltage correction and fault isolation capabilities of the HPR are verified, ensuring the normal operation of non-faulty ports.

6.2 Down-scale experimental test results

To further prove the effectiveness of the proposed HPR, a down-scale experimental prototype was built, as shown in Fig. 24. The grid fault is emulated by the programmable AC source, and the ESS is emulated by the DC source. The controller is implemented with DSP TMS320F28377.

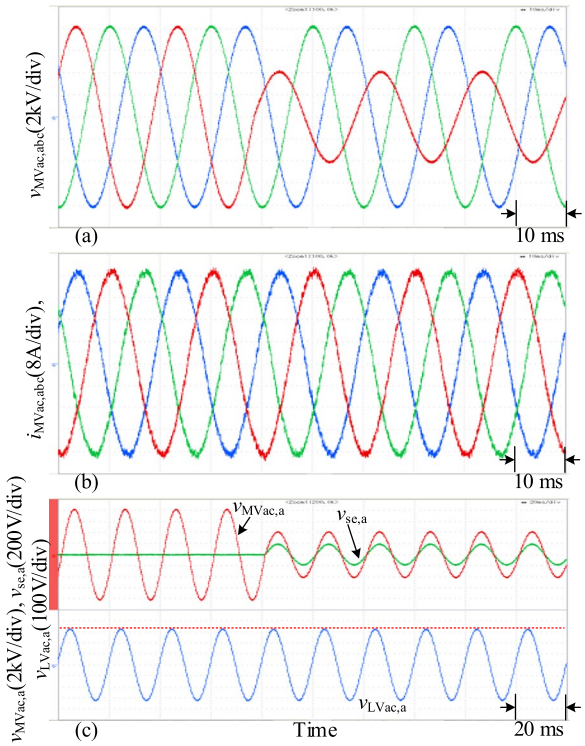

Fig. 22 Results of voltage support of the proposed HPR in an MVAC grid asymmetrical fault condition. **a** three-phase MVAC grid voltage; **b** three-phase MVAC current; **c** Phase A voltages at MVAC port, series winding, and LVAC port

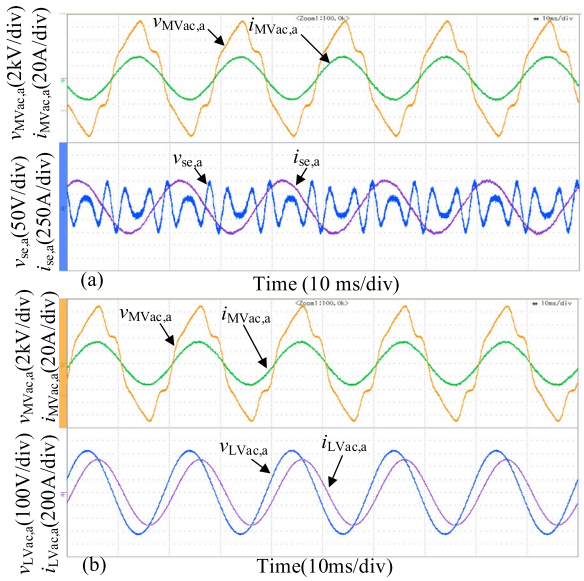

Fig. 23 Results of voltage correction of the proposed HPR in serious MVAC grid voltage distortion conditions. **a** Phase A voltage and current at MVAC and series winding ports; **b** Phase A voltage and current at MVAC and LVAC ports

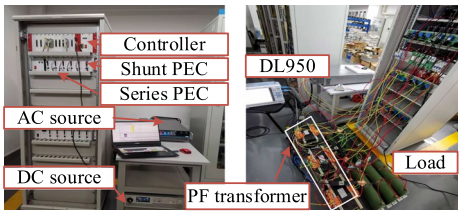

Fig. 24 Down-scale experimental test platform

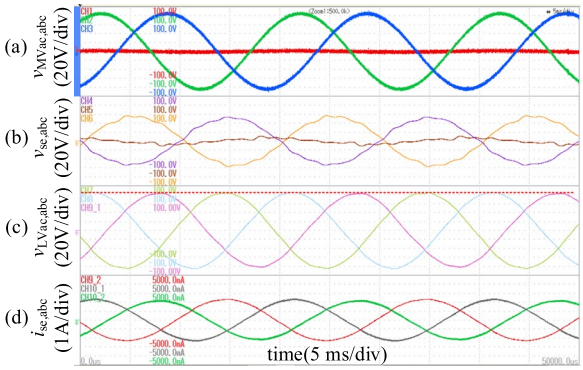

Fig. 25 Down-scale experimental results of voltage support of the proposed HPR in an MVAC grid asymmetrical fault with phase A 100% voltage drop condition. **a** three-phase MVAC grid voltage; **b** three-phase series PEC output voltage; **c** three-phase LVAC port voltage; **d** three-phase series winding current

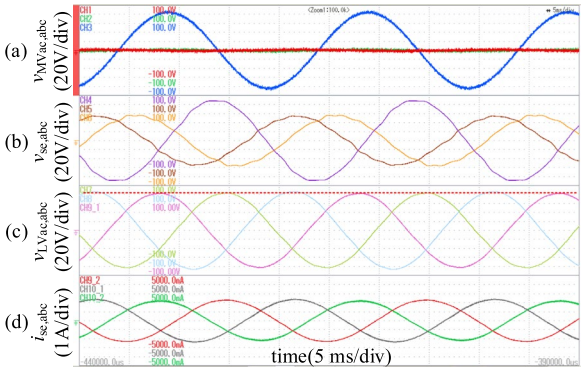

Fig. 26 Down-scale experimental results of voltage support of the proposed HPR during an MVAC grid asymmetrical fault with two-phase 100% voltage drop condition. **a** three-phase MVAC grid voltage; **b** three-phase series PEC output voltage; **c** three-phase LVAC port voltage; **d** three-phase series winding current

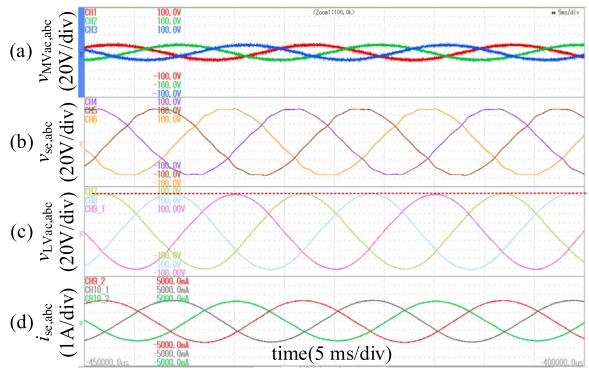

Fig. 27 Down-scale experimental results of voltage support of the proposed HPR in an MVAC grid symmetrical fault with three-phase 80% voltage drop condition. **a** three-phase MVAC grid voltage; **b** three-phase series PEC output voltage; **c** three-phase LVAC port voltage; **d** three-phase series winding current

The experimental parameters are as follows: the root mean square (RMS) value of the phase voltage at the MVAC port is 60 V; the RMS value of the phase voltage at the LVAC port is 60 V; the DC bus voltage is 200 V; the turn ratios of N_1, N_2, N_3, and N_4 are N_1: N_2: N_3: N_4 = 1.73: 1: 1: 1; the inductor and capacitor of the LC filter are 5 mH and 22 μF, respectively.

In the down-scale experimental test part, we focus on the fault isolation and voltage support performance of the HPR when the MVAC grid faults occur, thereby ensuring the healthy operation of the LVAC grid. The performance in an MVAC grid fault with 100% voltage drop of single-phase and two-phase, and 80% voltage drop of three-phase is investigated. Figures 25, 26 and 27 show the experimental results of the HPR in MVAC grid asymmetrical and symmetrical fault conditions with phase A 100% voltage drop, two-phase 100% voltage drop, and three-phase 80% voltage drop, respectively. When the voltage of the MVAC grid drops, the series PEC can be controlled to inject a support voltage (as shown in Figs. 25, 26 and 27b) to block the grid fault, ensuring that the LVAC grid operates in its pre-fault state and is unaffected by the MVAC grid disturbance, as shown inFigs. 25, 26 and 27c. Therefore, the fault isolation and voltage support capability can be well realized by controlling the series PEC of the proposed HPR during symmetrical and asymmetrical grid faults.

7 Conclusions

In this paper, an HPR scheme based on PF transformer electromagnetic coupling with PECs is proposed. The equivalent magnetic and electrical circuits of the novel PF transformer are established, and its working principle and port power flow are analyzed, with the control scheme presented. Based on theoretical analysis and simulation and prototype experimental tests results, the following conclusions are drawn.

(1) The series PEC of the HPR can actively regulate the voltage, and the shunt PEC can actively regulate the current. When combined with the active controls, the converters can realize flexible control of voltage and current at each HPR port to ensure that the voltages of the LVAC and LVDC grids are unaffected by the MVAC grid fault disturbance.
(2) With the PF transformer in the proposed HPR, only part of the power needs to be converted by the PECs of the HPR. Generally, no multi-level or multi-stage cascaded PEC structures are required, leading to simple topology and control complexity of the proposed HPR scheme.

Abbreviations

MVAC	Medium-voltage AC
LVAC	Low-voltage AC
LVDC	Low-voltage DC
HPR	Hybrid power router
PF	Power-frequency
PEC	Power electronic converters
SOGI	Second order generalized integrator
ESS	Energy storage system
SOC	State-of charge
CHIL	Controller hardware-in-the-loop

Acknowledgements
Not applicable.

Author contributions
JL: Conceptualization, Methodology, Software, Experiments, Investigation, Writing- Original Draft, Supervision. XY: Conceptualization, Validation, Formal analysis, Visualization, Writing—Original Draft. XY: Supervision, Writing: Review. JH: Experiments, Writing: Review & Editing. FX: Writing: Review & Editing.

Funding
This work was supported in part by the National Natural Science Foundation of China (Grant No. 52007010) and in part by State Key Laboratory of Advanced Electromagnetic Engineering and Technology (Grant No. AEET 2022KF003).

Availability of data and materials
Not applicable.

Declarations

Competing interests
The authors declare that they have no known competing financial interests or personal relationships that could have appeared to influence the work reported in this paper.

Received: 31 January 2023 Accepted: 18 August 2023
Published online: 05 September 2023

References

1. Ghosh, B., Chakraborty, A. K., & Bhowmik, A. R. (2023). Reliability and efficiency enhancement of a radial distribution system through value-based auto-recloser placement and network remodelling. *Protection and Control of Modern Power Systems, 8*, 1. https://doi.org/10.1186/s41601-022-00274-7
2. Yu, K., Li, J., Zeng, X. J., et al. (2022). Insulation parameter online measurement technology based on extended zero-sequence circuits for resonant grounding distribution networks. *IEEE Transactions on Power Delivery, 37*(6), 4679–4689.
3. Huang, K., Li, Y., Zhang, X., et al. (2021). Research on power control strategy of household-level electric power router based on hybrid energy storage droop control. *Protection and Control of Modern Power Systems, 6*, 13.
4. Huang, A. Q., Crow, M. L., Heydt, G. T., et al. (2011). The future renewable electric energy delivery and management (FREEDM) system: The energy internet. *Proceedings of the IEEE, 99*(1), 133–148.
5. Ali, S., Ling, Z., Tian, K., & Huang, Z. (2021). Recent advancements in submodule topologies and applications of MMC. *IEEE Journal of Emerging and Selected Topics in Power Electronics, 9*(3), 3407–3435.
6. Wang, D., Tian, J., Mao, C. X., et al. (2016). A 10-kV/400-V 500-kVA electronic power transformer. *IEEE Transactions on Industrial Electronics, 63*(11), 6653–6663.
7. Li, Y., Han, J., Cao, Y., Li, Y., Xiong, J., Sidorov, D., et al. (2017). A modular multilevel converter type solid state transformer with internal model control method. *International Journal of Electrical Power & Energy Systems, 85*, 153–163.
8. Bu, Z. M., Teng, J. X., Sun, X. F., et al. (2022). Low frequency voltage ripples decoupling with switched-capacitor conversion for an MMC-based SST. *IEEE Transactions on Industrial Electronics, 69*(11), 11293–11303.
9. Zhou, J., Zhang, J., Wang, J., Zang, J., & Cai, X. (2021). Design and control of power fluctuation delivery for cell capacitance optimization in multi-port modular solid-state transformers. *IEEE Transactions on Power Electronics, 36*(2), 1412–1427.
10. Huber, J. E., & Kolar, J. W. (2014). Volume/weight/cost comparison of a 1MVA 10 kV/400 V solid-state against a conventional low-frequency distribution transformer. In *2014 IEEE energy conversion congress and exposition (ECCE)*, Pittsburgh (pp. 4545–4552).
11. Liu, Q., & Li, Y. (2020). An inductive filtering-based parallel operating transformer with shared filter for power quality improvement of wind farm. *IEEE Transactions on Power Electronics, 35*(9), 9281–9290.
12. Li, Y., Peng, Y., Liu, F., Sidorov, D., Panasetsky, D., Liang, C., et al. (2017). A controllably inductive filtering method with transformer-integrated linear reactor for power quality improvement of shipboard power system. *IEEE Transactions on Power Delivery, 32*(4), 1817–1827.
13. Lai, J., Yin, X., Zhang, Z., Wang, Z., & Yin, X. (2019). System modeling and cascaded passivity based control for distribution transformer integrated with static synchronous compensator. *International Journal of Electrical Power & Energy Systems, 113*, 1035–1046.
14. Lei, E., Yin, X., Zhang, Z., & Chen, Y. (2017). An improved transformer winding tap injection dstatcom topology for medium-voltage reactive power compensation. *IEEE Transactions on Power Electronics, 33*(3), 2113–2126.
15. Aeloiza, E. C., Enjeti, P. N., Moran, L. A., & Pitel, I. (2003). Next generation distribution transformer: to address power quality for critical loads. In *IEEE 34th annual conference on power electronics specialist*, Acapulco, Mexico (pp. 1266–1271).
16. Cai, G., Wang, Y., Liu, C., et al. (2020). Direct AC/AC conversion based hybrid distribution transformer with two-phase supported regulation. *Electric Power Automation Equipment, 40*(12), 8–17.
17. Lee, H. J., Yoon, S. W., & Yoon, Y. D. (2022). Hybrid distribution transformer based on an existing distribution transformer and a series-connected power converter. *IEEE Transactions on Power Delivery, 37*(5), 4202–4211.
18. Zheng, L. R., Marellapudi, A., Chowdhury, V. R., Bilakanti, N., Kandula, R. P., et al. (2022). Solid-state transformer and hybrid transformer with integrated energy storage in active distribution grids: Technical and economic comparison, dispatch, and control. *IEEE Journal of Emerging and Selected Topics in Power Electronics, 10*(4), 3771–3787.
19. Zhao, X. J., Liu, Y. R., Chai, X. H., et al. (2023). Multimode operation mechanism analysis and power flow flexible control of a new type of electric energy router for low-voltage distribution network. *IEEE Transactions on Smart Grid, 13*(5), 3594–3606.
20. Elsaharty, M. A., Candela, J. I., & Rodriguez, P. (2018). Power system compensation using a power electronics integrated transformer. *IEEE Transactions on Power Delivery, 33*(4), 1744–1754.
21. Chen, Z., Li, H., Liu, L., Xiang, L., & Bai, B. (2019). Dc bias treatment of hybrid type transformer based on magnetic flux modulation mechanism. *IEEE Transactions on Magnetics, 55*(6), 1–4.
22. Yang, B., Zhao, J. F., Ji, Z. D., et al. (2020). Overview of hybrid transformer technologies. *Electric Power Automation Equipment, 40*(02), 205–213.
23. Liu, Y., Liang, D., Wang, Y., Kou, P., & Yang, C. (2021). Power flow analysis and dc-link voltage control of hybrid distribution transformer. *IEEE Transactions on Power Electronics, 36*(11), 12579–12595.
24. Liu, Y. B., Zhang, L. S., Liang, D. L., et al. (2022). Quasi- proportional-resonant control for the hybrid distribution transformer with LCL-type converters. *IEEE Transactions on Industry Applications, 58*(5), 6368–6385.
25. Yang, R. H., & Jin, J. X. (2021). Unified power quality conditioner with advanced dual control for performance improvement of dfig-based wind farm. *IEEE Transactions on Sustainable Energy, 12*(1), 116–126.
26. Rodriguez, P., Teodorescu, R., Candela I., et al. (2006). New positive-sequence voltage detector for grid synchronization of power converters under faulty grid conditions. In *37th IEEE power electronics specialists conference* (pp. 1–7).
27. Li, Z., Sheng, W. X., Duan, Q., et al. (2019). Coordinated control strategy of AC/DC hybrid power router based on voltage stabilization by energy storage. *Automation of Electric Power Systems, 43*(2), 121–129.
28. Chen, X., Yan, L. F., Zhou, X., et al. (2018). A novel DVR-ESS-embedded wind-energy conversion system. *IEEE Transactions on Sustainable Energy, 9*(3), 1265–1274.

Jinmu Lai received the B.S. and M.S. degree in electrical engineering and the Ph.D. degree from the Huazhong University of Science and Technology, Wuhan, China, in 2014, 2017, and 2020, respectively. He is currently a Lecturer with the School of Electrical and information Engineering, Zhengzhou University, Zhengzhou, China. His research interests include power router, power quality control, and the application of power electronics in power systems.

Xin Yin received the B.Eng. degree in electronic engineering from the University of Sheffield, U.K., in 2008, the M.Sc. degree in Telecommunication from University College London, U.K., in 2009, and the Ph.D. degree in electrical and electronic engineering from the University of Manchester, U.K., in 2016. He is a lecturer in school of automation, Wuhan University of Technology now. His current research interests include control and protection of distribution system with renewable energy and power electronic technology and device and its application in power system.

Xianggen Yin received the B.S., M.S., and Ph.D. degrees in electrical engineering from Huazhong University of Science and Technology (HUST), Wuhan, China, in 1982, 1985 and 1989, respectively. He is now a Professor in the School of Electrical and Electronic Engineering, HUST. His research interests include protective relaying, power system stability control and power electronics.

Jiaxuan Hu received the B.S. degree in electrical engineering from the Chongqing University in 2020. He is currently pursuing the Ph.D. degree at the Huazhong University of Science and Technology, Wuhan, China. His research interests include power router and the application of power electronics in power systems.

Fan Xiao received the Ph.D. degree from the Huazhong University of Science and Technology, Wuhan, China, in 2017. He is currently an engineer at State Grid Hubei Electric Power Research Institute, Wuhan, Hubei Province. His research interests include protective relaying, power system stability control and power electronics.